

Invited Paper

Characterization of the noise behavior in lens-integrated CMOS terahertz video cameras

Robin Zatta *, Ritesh Jain and Ullrich Pfeiffer
Institute for High-frequency and Communications Technology,
University of Wuppertal, Germany
* Email: zatta@uni-wuppertal.de

(Received October 03, 2018)

Abstract: This paper reports on the detailed experimental investigations of the NEP behavior in 1k-pixel terahertz video camera module implemented in 65nm CMOS technology which can act as THz imager or power meter. The NEP is characterized for both operation modes, imaging and power metering, for different frame rates, averages, and clipping windows, to understand the trade-off impacts of different camera operation modes on the camera sensitivity for both modes and their limitations. Mean offset and noise trends are also investigated over time in a temperature-controlled environment to analyze the camera performance under long integration periods which show that a warm-up time of 60 minutes should be respected for very accurate measurements. Moreover, our results verify that the averaged single pixel real-time NEP is relatively stable over different readout frame rates and shows a minimum typical NEP at 822 GHz of 17 nW for different frame rates, within the wide 3-dB bandwidth between 740 and 930 GHz and hence, the minimum NEP for 1 second integration time at a frame rate of 30 fps is 3.1 nW. This means that a 100 pW THz signal can be detected for an integration time of 31 seconds, respectively. The single pixel NEP can be further improved through averaging over K frames due to a noise reduction by \sqrt{K} , which is helpful by using the camera module as an imager. Thereby, the RMS pixel noise is integrated over the whole video bandwidth which is limited by a LPF with a cut-off frequency of 150 kHz. For determining NEP, the R_V is measured through a 26-dBi illumination source from 0.6 to 1.1 THz. Using the camera in power meter mode the NEP increases by \sqrt{N} for selecting N pixels at the readout and hence, the typical minimum NEP for the whole frame is 544 nW for different frame rates. This can also be improved through integration and the single pixel performance can be reached again after 60 seconds which corresponds to an average of 1800 frames. Thereby, the fixed pattern noise has to be measured periodically due to thermal drifts for long integration periods because otherwise the noise and hence, NEP saturates. Furthermore, the directivity of the pixels is analyzed and shows that it decreases from center to outer pixels due to the change in effective aperture at offset locations of the optical axis but most of them are still in a 3-dB range. For best performance the signal should be centered with respect to the image.

Keywords: Sub-millimeter imaging, Terahertz direct detection, Terahertz imaging, Noise, NEP, Silicon lens

doi: [10.11906/TST.102-123.2018.12.10](https://doi.org/10.11906/TST.102-123.2018.12.10)

1. Introduction

Terahertz (THz) technology has witnessed an increased research and commercial interest in the

recent past [1]. Today, many cameras operating in the THz range have been developed [2-4]. Possible applications for these cameras are imaging, including diffused, active imaging [5], light-field imaging [6], passive imaging [7], and single or multipixel power metering. Novel applications are also quickly emerging, such as using the light-field mapping at the camera [6] for spectral analysis by applying external diffraction gratings to match frequencies to different entering angles at the camera aperture, such as shown in [8].

Due to the general lack of high power radiation sources in 0.3 to 3 THz band, THz detectors have to be extremely sensitive. Therefore, designing detectors with an ultra-low noise equivalent power (NEP) becomes a major challenge in this field. For a THz camera, consisting of a multi-pixel focal plane array (FPA) of detectors, the averaged pixel NEP is determined by the RMS image noise and the overall responsivity (R_V) [2]. Hence, the camera module must be optimized for both the parameters, RMS image noise and R_V . In theory, for integrating over more than one pixel the noise worsens with increasing number of pixels due to the statistical error propagation. However, the imaging aperture also improves which in principle can be used to collect more power, subjected to the maximum power and numerical aperture limitations from the source. The increased NEP for a larger readout window can be reduced again through frame averaging what corresponds to integrating over time.

The investigated camera module in this paper can be used in two different operation modes. First, by using the camera in the '*imaging mode*', it can act as a multipixel imager as shown in [2, 6-7] and in this relation, the single pixel NEP is determined by its R_V and RMS pixel noise. Thereby, the RMS image noise can be used to calculate an averaged NEP which is only validated for the case of normal distributed RMS pixel noise for the whole frame. Second, by using the '*power meter mode*' the RMS frame noise is the significant parameter because here noise scales with the number of pixels which are used at the readout. This will be explained in a more detailed way in the corresponding section.

This paper reports for the first time on the detailed characterization of the NEP behavior of the 1 k-pixel THz video camera implemented in 65nm bulk CMOS technology which was developed by TicWave GmbH [9] based on the detector array chip presented in [2]. In this paper, the RMS image noise variation for different frames rates, averaging factors, and measurement time, is examined carefully to understand the optimum performance mode of the camera under different conditions for both imaging and power metering.

The organization of this paper is as follows. Section 2 presents the camera architecture briefly, explaining the readout functionality and the different adjustments which are possible via programming the serial interface of the camera module, gives an introduction about how noise is generated in CMOS THz cameras, and explains how an image is translated from the object plane to the image plane for a lens-integrated detector array. In section 3, an extended experimental analysis of the camera module's NEP performance in video-mode is reported for both operation

modes. The RMS pixel noise as well as the RMS image noise are characterized for different frame rates, frame averages and clipping windows. Furthermore, the RMS frame noise for an increasing clipping window is characterized. In this context, the relation between mathematical theory and measurement results is also discussed. Moreover, the camera R_V is measured in the 0.7 to 1.1 THz band through an CW illumination source. Furthermore, the relative directivities for different camera pixels are measured for the very first time in this paper. Besides, the time trend for the noise and mean offset in a temperature-controlled environment is analyzed for a 5-hours continuous operation period to figure out the performance behavior over long measurements. The conclusions are summarized in section 4.

2. THz-Camera

The THz-Camera has been developed by TicWave GmbH based on the detector array presented in [2], and it includes a correlated double sampler to reduce the low frequency noise. It can be operated in video mode with frame rates between 1 and 60 frames per second (*fps*) and the programmable readout is done through a USB interface. For the readout, a desired frame rate and a desired clipping window at the FPA can be chosen individually. By setting a clipping window N pixels can be selected in an $n \times m$ -array for the readout which improves the measurement time $1024/N$ times. Note that the vendor offers a graphical software for video streaming and image capture where such adjustments can also be done in a user-friendly manner (see Fig 1).

2.1 Camera module architecture

The 32×32 -pixel array consists of 1024 differential on-chip ring antennas coupled to NMOS direct detectors operated above their cut-off frequency [2]. The operation is based on the principle of distributed resistive self-mixing. The camera module, packaged in a $5 \times 5 \times 5$ cm³ housing, as well as the TeraCam GUI are shown in Fig.1. Note that the chip is glued to the backside of a 41.7-dBi hyper-hemispherical silicon lens (measured at 850 GHz) for backside radiation and connected to a PCB through wire-bonding. The analog signal processing is done on the PCB where the detector output gets measured by a correlated double sampler (CDS). The detector output signal is also amplified in three stages. First, a pre-amplifier is implemented, on which the CDS follows with a gain of 2 and finally, additional gain and the offset can be adjusted in the third stage at an ultra-low noise amplifier. With these adjustments the working range of the camera module can be determined. At the moment, it is optimized to detect signals that lie extremely close to the noise floor, which is the most challenging case for THz imaging for to low-power THz sources.

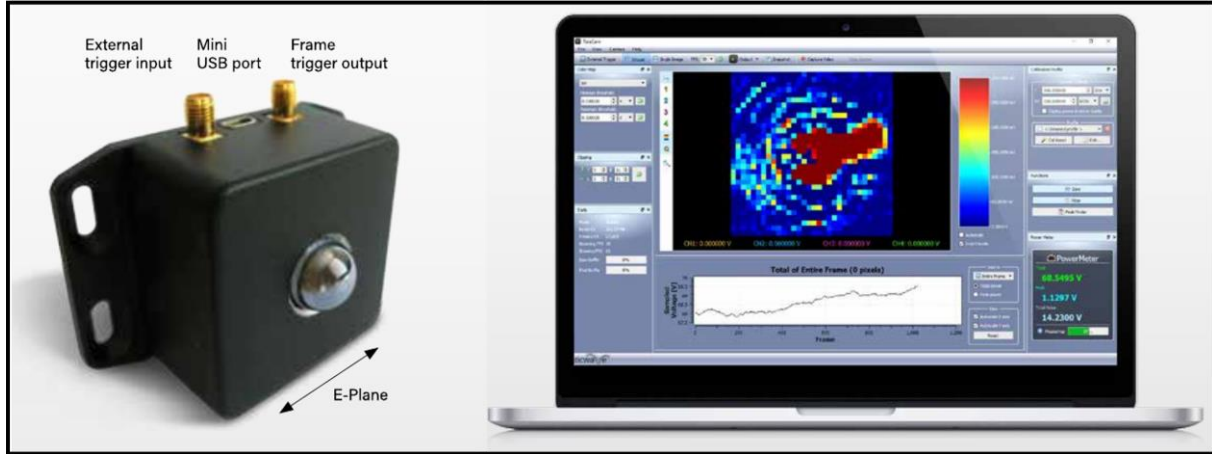


Fig. 1 Picture of the camera module on the left packaged in a $5 \times 5 \times 5 \text{ cm}^3$ housing and the software provided by TicWave GmbH on the right (from [9]).

2.2 Noise in THz CMOS cameras

Noise in CMOS cameras is not only determined by the transistor but also by the readout chain. Transistor noise is composed of thermal noise, flicker noise and shot noise. Thermal noise is given by

$$V_{n,th} = \sqrt{4k_B T R \Delta f}, \quad (1)$$

where T is the temperature, R the resistance and Δf the bandwidth (BW). In the camera, thermal noise is integrated over the whole video bandwidth of the camera readout which is limited by a low pass filter before the CDS. The video bandwidth is optimized for the preferred frame rate. In current implementation, the video bandwidth limit at the investigated THz-Camera is adjusted at 150 kHz to perform optimally until a frame rate of 30 fps . As described in [10], thermal noise has nearly normal amplitude distribution and can be reduced by averaging. Additionally, switching noise also comes up through the amplifiers and the 16-bit ADC. Moreover, CMOS cameras have a fixed-pattern noise (FPN) which is caused by different mean offsets for the on-chip-detectors pixels due to process variation but this can be calibrated out measurement subtraction. The FPN will be cancelled out at the beginning of each measurement to minimize the effect of chip manufacturing process on the results.

2.3 Measurement basics

The camera chip is glued to the backside of a hyper-hemispherical silicon lens with a radius $R = 75 \text{ mm}$. From [6] we know that the field-of-view is $\pm 23^\circ$ in both E- and H-Plane for a lens extension length of $X = 2.83 \text{ mm}$ and hence, the X/R ratio of the lens is 0.377, which corresponds to a close-to-elliptical extension with maximum diffraction-limited directivity [11]. Due to off-axis properties of silicon dielectric lens antennas [12], each pixel holds an individual

directivity, which decreases for an off-axis pixel and should be worst for the corner pixels. This paper reports for the very first time on the change in directivity for each of the 1024 pixels of the investigated camera module. The image projection onto the detector chip through collecting the incoming beam into the hyper-hemispherical silicon lens works as visualized and described in Fig 2.

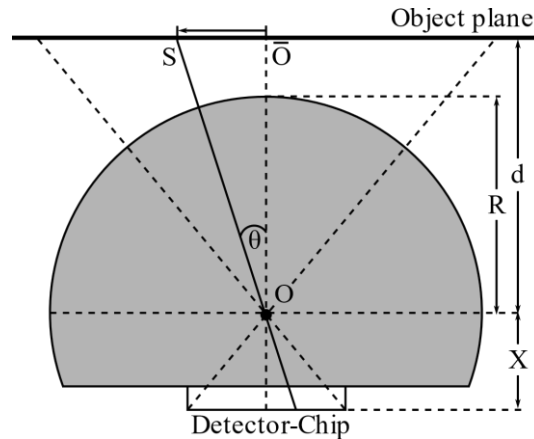


Fig. 2 Simplified geometrical optics transformation from image plane to the detector chip. The point S on the object plane at an incidence angle θ is projected to a point x on the image plane. The lens optical axis is marked as $\bar{O}O$ where O indicates the center of the lens. The distance between lens center and the object plane is denoted as d , R indicates the lens radius, and the X the lens extension length (from [6]).

Due to the pixel-to-angle dependency of the incoming beam, the camera module can be used for more applications than just imaging or power metering. Additional applications include using the camera as a 1D-array for THz spectroscopy as demonstrated in [8] where an external diffraction grating assigns each frequency a certain angle and thus, each pixel corresponds to this entering angle. Light-field imaging as explained in [6] is another interesting application which is possible with the camera where, for example, a radiation pattern can be measured through driving in a 2D-plane. This theory is also used for measuring the R_V of the camera module which is explained later. If the radiation source is placed extremely close to the camera in a back-to-back configuration, an assumption can be made that the whole power enters into the silicon lens, considering the model in Fig 2.

3. Performance measurement results

This section investigates the overall NEP or noise performance of the 1 k-pixel THz-camera in video mode. The NEP is the noise equivalent input power for an $SNR = 1$ at the detector output. For all pixels operated in video mode, the noise is integrated over the whole 150 kHz video bandwidth. The averaged pixel NEP which is an important parameter for THz imagers can be calculated from the overall R_V and the RMS image noise. This will be explained later in more

details. It will be investigated to see how the minimum real-time NEP of 17 nW at 822 GHz (see Fig 3) including noise integrated over the whole video bandwidth can be improved through averaging or clipping. The measured NEP trend over for the frequency band between 0.6 and 1.1 THz is shown for a frame rate of 30 fps at 822 in Fig3.

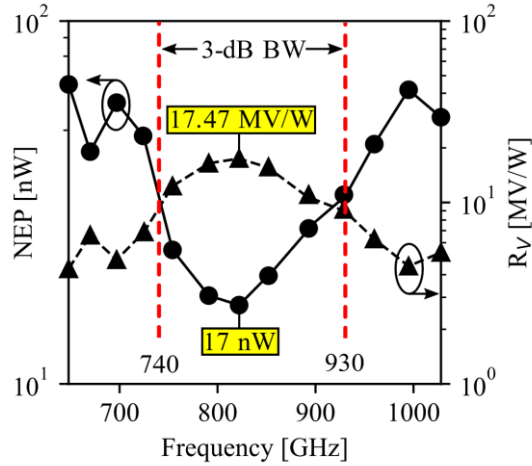


Fig. 3 NEP trend for the 0.6 to 1.1 THz band. The minimum NEP of 16.48 nW within the 190 GHz 3-dB bandwidth is measured for a frame rate of 1 fps at 822 GHz in a back-to-back measurement, the maximum R_V is 17.47 MV/W . Thereby, the amplifier gain is not de-embedded from the R_V and noise, but cancelled out for NEP. The setup as well as the measurement routine is explained later.

It has to be mentioned that the 3-stage amplifier gain is not de-embedded from both noise and responsivity for all measurements shown in this paper and hence, values in a range of MV/W for R_V and mV for noise are expected but the gain is cancelled out for the calculation of NEP which will be described later in a more detailed way.

This section is organized as follows. Relevant noise values for both imaging and power meter mode are analyzed in sections 3.1 and 3.2 which split further into sections. Thereby, corresponding RMS pixel noise and RMS image noise are shown in sections 3.1.1 and 3.1.3, respectively and pixel directivity is also characterized in section 3.1.2. Section 3.2 discusses the impact of frame clipping or windowing on the noise, examining the use of camera module as single pixel (3.2.2) or multipixel (3.2.1) power meter. In section 3.4, the RMS image noise is also characterized for different frame rates. In this context, R_V is also measured due to a change over the frame rate. Additionally, for the typical chosen video mode of 30 fps , the noise versus integration time is analyzed in section 3.5 for both the whole frame and a single image to judge the optimum mode for imaging and power metering. Finally, section 3.6 examines the time-drifts of camera mean offset and noise in a temperature-controlled environment.

Note that formulations use the following notation for pixel response: The pixel response is given by $V_{i,k}$ for pixel coordinates with the vector index $i \in \{0, N\}$ at frame $k \in \{0, K\}$, where N and

K are the number of selected pixels at the camera readout and the number of recorded frames, respectively.

3.1 Imaging mode

The camera module can be used as a THz imager as demonstrated in [2]. For imaging, the individual single pixel NEP is relevant because here, each pixel works as a separate sensor. To figure out the single pixel NEP of each pixel, the RMS pixel noise and the pixel responsivity $R_{V,i}$ have to be measured. These characterizations are shown in the following.

3.1.1 RMS pixel noise

RMS pixel noise shows the individual noise of each pixel after performing an offset cancellation which is necessary to calibrate out the FPN. First, it is important to figure out the distribution of a single pixel to know if noise is dominated by thermal noise or other components (we know from [10] that thermal noise has a nearly gaussian distribution). Furthermore, the investigation of the RMS pixel noise for all pixels of the camera module shows how noise is locally distributed over the 32×32 -pixel array to figure out if local imaging areas result in a better NEP through lower noise. The RMS image noise which will be discussed in the section 3.1.3 shows an averaged RMS pixel noise over the whole array but this is only validated if the RMS pixel noise and mean offsets are normally distributed. Thus, for this investigation the distribution of the RMS pixel noise also has to be examined.

To characterize the RMS pixel noise of the camera module, a measurement matrix V_{30fps} with a total of $2^{16} = 65536$ frames are recorded at 30 fps via the USB interface which takes 36 minutes . The RMS pixel noise is determined for each pixel of the frame individually. It has to be mentioned that all pixels are selected for the readout and hence, out of this matrix, the RMS pixel noise is determined in post-processing. It would also be possible to select just a single pixel for the readout but this is not shown here. The distribution for a sample pixel is shown in Fig 4 (d) and the noise of each single pixel is plotted in a 2D-image-representation, to figure out if there exists any dependency on the location or if there is an identifiable interlocking between neighbor pixels. This is additionally shown in a histogram plot in Fig 4 (c).

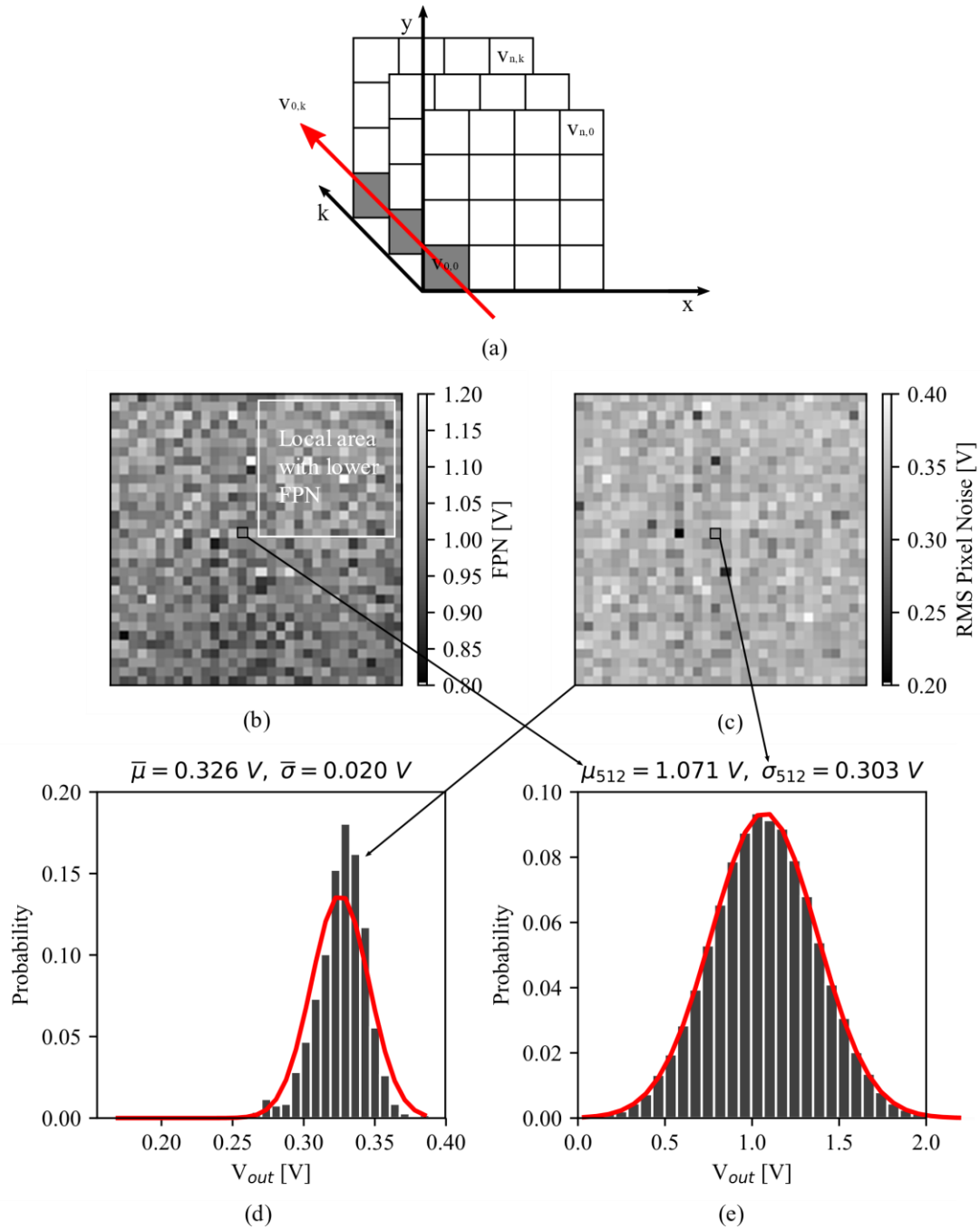


Fig. 4 (a) Graphical representation of RMS pixel noise for 2^{16} frames, (b) FPN and (c) RMS pixel noise σ_i for the whole frame plotted in a 2D-image-plot, (d) the distribution of the pixels in a histogram plot and (e) the distribution of a center pixel.

The RMS pixel noise σ_i can be extracted from the measurement matrix V_{30fps} by using the following equation from [13] as:

$$\sigma_i = \sqrt{\frac{1}{K-1} \sum_{k=1}^K (V_{i,k} - \mu_i)^2} \quad (2)$$

with

$$\mu_i = \frac{1}{K} \sum_{k=1}^K V_{i,k}, \quad (3)$$

where μ_i is the individual pixel FPN (shown in Fig 4 (b)) and $V_{i,k}$ is the response of pixel i at image k (total number of frames, here $k = 2^{16}$). As explained in section 2.2, FPN is cancelled out for each of the following measurements. This is essential due to non-normally distributed FPN and, for example, for averaging the whole frame a reduction in noise can be just reached for normally distributed noise which lies around 0. This means that the FPN cancellation for pixel 512 in Fig 4 (a) can be obtained by shifting the distribution to 0 (subtract μ_{512}). Later, it will be also investigated how valid the FPN cancellation is for long-term measurements where thermal drifts could impact.

Moreover, this investigation shows that the noise is randomly located in the camera and hence, there are no preferred areas identifiable for imaging or power metering based on this. The individual RMS pixel noise is closely but not perfectly normally distributed. This leads to the assumption that RMS pixel noise as well as RMS frame noise can be improved by integration over time. The maximum pixel-to-pixel variation is $\bar{\sigma}/\bar{\mu} = 6.1\%$ in the $1-\sigma$ region, which is identifiable out of the sigma to offset ratio (see Fig 4 (b)). The next parameter which can influence the individual pixel NEP is the pixel directivity and hence, this will be characterized in the following section.

3.1.2 Pixel directivity

As previously explained, a THz camera has to perform well for both parameter noise and R_V . The RMS pixel noise has been investigated in the previous section. Based on this no preferable locations are identifiable and now the pixel directivity is analyzed to see how this influences the pixel NEP. For this analysis a measurement is performed where the camera is mounted onto the U5R robot arm, which allows precise 3D movements, and just a single pixel gets illuminated through a x54 multiplier chain source from AB Millimetre coupled to a 26-dBi (at 850 GHz) horn antenna radiating around 8 μW in the 0.6 to 1.1 THz band at a distance of 30 cm. The camera is rotated circularly around 0° (see Fig 5 (a)) for an opening angle of $\pm 30^\circ$ with a step size of 0.5°. At each position of the robot arm in the 3D-movement an averaged frame is recorded at the camera. This means that each pixel gets measured at each position and hence, a radiation pattern for each pixel can be done by performing just a single measurement. In post-processing, the maximum for each pixel is determined and the change in directivity can be derived as the pixel deviation in respect to the maximum pixel. Note that the pixel variation is given by its RMS pixel noise but this is randomly located. However, the directivity shows a local dependency with a maximum for the center pixels and decreases to the edges where the corner pixels show a minimum of -9 dBi which

is expected (read section 2.3). The measurement setup and results are shown in Fig 5.

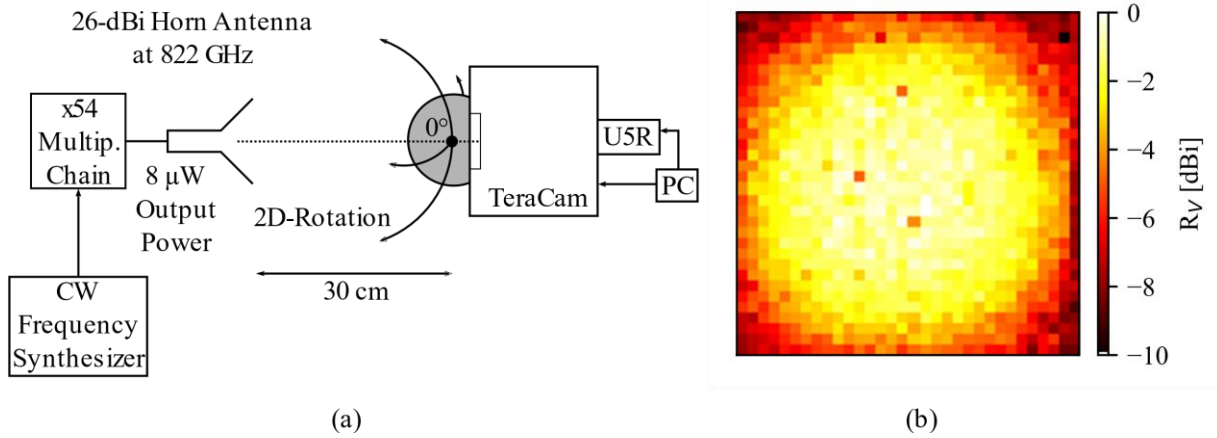


Fig. 5 (a) Measurement setup for determining the individual $R_{V,i}$ for each pixel. Through rotation for both angles, theta and phi, around 0° each pixel gets illuminated for a certain position of the robot arm (b) voltage response plotted in a dBi-scale for each pixel in a contour plot where each pixel is shown with respect to the maximum pixel.

This measurement verifies that the directivity for off-axis pixels worsens but most of the pixels are still in a 3-dB range. This also explains why images in [2] are mostly shown in this region where directivity is still in the 3-dB range as visualized in Fig 5 (a). This measurement data could be used as a calibration data for the camera pixels. With respect to the RMS pixel noise this also means that the NEP for inner pixels is higher than for outer ones and hence, for imaging as well as power metering the radiation should always be focused on the inner part of the camera. Out of this measurement matrix and the results from Fig 4 (c), where the individual RMS pixel noise was analyzed, the stability of the silicon technology in relation to the pixels' NEP can be determined. Therefore, a 10 x 10 clipping window is chosen. The responsivity shows a $1-\sigma$ deviation of 10 percent, the noise a $1-\sigma$ deviation of 6 percent and the NEP a $1-\sigma$ deviation of 10 percent pixel-to-pixel variation.

3.1.3 RMS image noise

The RMS image noise describes the averaged image noise referred to a single pixel as explained in [14] and is a well-known standard parameter to characterize the averaged pixel NEP of THz cameras which is just validated if the pixel noise is normally and randomly located over the whole frame. The RMS image noise is calculated from the measurement matrix V_{30fps} (see section 3.1) and can be calculated as the standard deviation

$$\sigma_k = \sqrt{\frac{1}{N-1} \sum_{i=1}^N (V_{i,k} - \mu_k)^2} \quad (4)$$

with the mean offset close to zero due to cancelled out FPN

$$\mu_k = \frac{1}{N} \sum_{i=1}^N V_{i,k}, \quad (5)$$

where $V_{i,k}$ is the voltage response of a single pixel and N is the number of the pixels selected at the camera module. The larger the number of samples for determining σ_k is, the more precise is the RMS image noise due to lower statistical noise. The RMS image noise can be calculated for each image in V_{30fps} and hence, also be plotted into a histogram representation which is shown in Fig 6. This gives an indication about the deviation in the RMS image noise. In this histogram plot, the distribution is fitted by a normal distribution (red line).

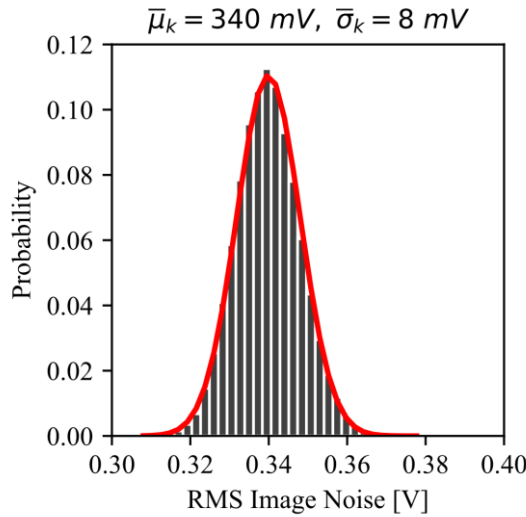


Fig. 6 Distribution of the RMS image noise calculated for each frame out of V_{30fps} and plotted into a histogram plot.

The RMS image noise shows a normal distributed behavior with a deviation of 8 mV . Thereby, $\bar{\mu}_k$ is the mean RMS image noise and $\bar{\sigma}_k$ the deviation of the RMS image noise.

This gives us now an indication about the variation in the RMS image noise. On average, the RMS image noise for a frame rate of 30 fps is 340 mV . This also means that the NEP values are varying in a range of $\bar{\sigma}_k/\bar{\mu}_k = 8/340 = 2.3\%$ for the chosen frame rate of 30 fps .

3.2 Power meter mode

Power meters for THz radiation are mostly single detectors based on physical principles as pyroelectric, opto-acoustic pneumatic or calorimetry. The problem is that these kind of power meters detect also infrared waves and for blocking them expensive filters are needed. Through a limited RF BW a THz camera which consists of a detector array offers a cheap solution for accurate

power metering. The performance of a terahertz direct detector array is typically expressed by means of R_V and noise equivalent power (NEP) [2]. The R_V is given by the ratio between total camera voltage response and incoming power into the silicon lens; and NEP by the ratio of noise voltage and R_V as follows:

$$V_{out} = \sum_{i=1}^N V_i - \mu_i, R_{V,k} = \frac{V_{out}[V]}{P_{in}[W]}, NEP_{opt} [W] = \frac{\sigma_k [V]}{R_{V,k} \left[\frac{V}{W} \right]}, \quad (6)$$

where the total camera voltage response is the integrated over the zero-offsetted camera response. Along with to using the camera module for THz imaging [2, 6-7], it can also act as a single pixel or multipixel power meter in a calibrated format. Hereby, the camera has to be calibrated through a THz illumination source with known power. Using the camera module as a single pixel power meter is sensible if it is possible to focus back the whole power into a single pixel. For a truly parallel beam, or a far-away source, this should be possible. In many cases more than one element of the pixel array gets illuminated and in this case the camera can also act as a multipixel power meter, but through selecting a larger number of pixels for the readout noise also worsens. Hence, the noise for different clipping windows is characterized in the following to figure out if noise scales as expected in theory and how it can be improved by averaging over a number of frames.

3.2.1 RMS frame noise

Adding N independent sources of Gaussian noise for multipixel power metering yields

$$\sigma_F = \sqrt{\sum_{i=1}^N \sigma_i^2} \approx \sqrt{N} \cdot \sigma_k, \quad (7)$$

which can be explained by error propagation described in [13]. Thereby, σ_F represents the RMS frame noise for a selected clipping window at the camera readout. The RMS frame noise and hence, the NEP , worsens for an increased pixel count by \sqrt{N} . This leads to the fact that the clipping window should be chosen optimally in a way that just the pixels which show a response are read out.

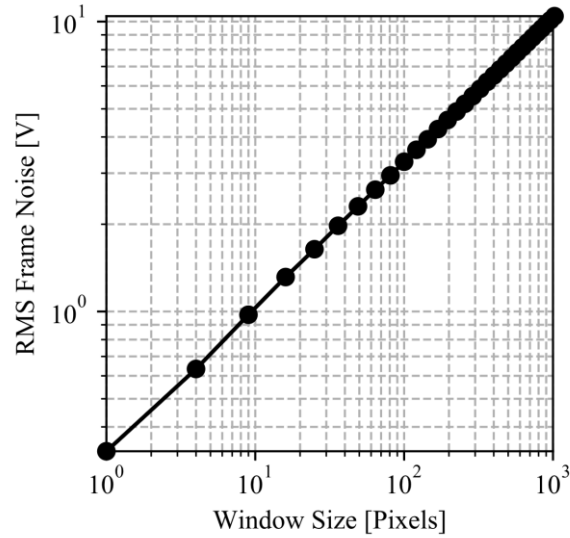


Fig. 7 The measured RMS frame noise for different window sizes is plotted for a frame rate of 30 *fps* and an average of 2^{16} frames calculated by the left term of the equation in formula (8). A progressive trend is visible in this log-log representation.

To compare theory and measurements here, the RMS frame noise is calculated from the measurement matrix V_{30fps} (matrix architecture shown in Fig 3 (a)) for different clipping windows with a size of $(2^1, \dots, 2^{10})$ pixels. This is done for each image in V_{30fps} and the results of post-processing work are shown in a log-log representation in Fig 7 for an average of 2^{16} frames. It is visible that the average for each window size follows a progressive trend in this log-log representation with a slope of $1/2$ which means that there is an increase of $\sqrt{2}$ per data point shown in Fig 7. This matches the theory of adding N independent sources of Gaussian noise and hence, the RMS image noise can be scaled with the previously explained factor of \sqrt{N} . Finally, this means that the estimation for the NEP by calculating the RMS image noise is still valid for the investigated THz-Camera. The findings of this characterization tell us that it is best to select the smallest possible clipping window for power metering. This also benefits a smaller measurement time because, for reading out N pixels the measurement time decreases by a factor of $N/1024$ and hence, the NEP can be additionally improved through larger averaging factor for the same measurement time. If the camera module is used as a multipixel power meter just those pixels have to be selected for the readout which show us a signal because this results in the best estimate through a lower noise. This can be done by doing a reference measurement and setting a threshold for later pixel selection at the power measurement.

3.4 NEP versus frame rate

As explained in section 2.1, the video camera can be used for different frame rates in a range from 1 to 60 frames per second. Detection of extremely small THz signals can be challenging in many cases and we are searching for the optimum operation mode of the camera module. Because

the frame rate shows a variance in RMS image noise and R_V , too, both the parameters are investigated in this section. Applying a smaller frame rate would result in a larger measurement time but this might not be critical if the NEP can be improved to detect these small signals.

The RMS image noise and R_V for the different frame rates are measured to investigate if there is any benefit for the NEP by applying a lower frame rate. Therefore, images for the available frame rates of $FPS = (1, 2, 3, 4, 5, 6, 7.5, 10, 12, 15, 20, 30, 60)$ are readout iteratively 4096 *times* each, for both noise and R_V . The plotted RMS image noise values in Fig 8 (a) are then the mean RMS image noise values explained in section 3.1.1 (see $\bar{\mu}_k$ in Fig 6) to show a smoother trend. Responsivity is measured in a back-to-back measurement as shown in Fig 6 (a), for determining the corresponding noise the same measurement is repeated without applying any illumination. The resulting matrix F_{30fps} contains 4096 frames for each frame rate, the RMS image noise as well as the R_V are plotted over frame rate in Fig 6 (b), and NEP is plotted in Fig 6 (c).

For the R_V measurement, it is assumed that the whole power enters the silicon hyper-hemispherical lens of the camera module which gives a good estimation for the R_V . As visualized in Fig 8 and also well-known in optics rays which enter the lens at an angle $\neq 90^\circ$ get reflected to a certain extend and at a critical angle the ray gets reflected completely. Then, due to the assumption of collecting the whole power with the camera module the R_V gets slightly underestimated. But the power within the half power beam width (HPBW) should enter the lens almost complete and hence, the error should be negligible.

At this point, it has to be mentioned that the amplitude noise for increased input power into the lens does not show an impact. This can be explained because the output power of $8 \mu W$ is not large enough. RMS pixel noise can be derived from the pixel amplitude by measuring the amplitude for a number of times and calculating the sigma as explained in section 3.2.1.

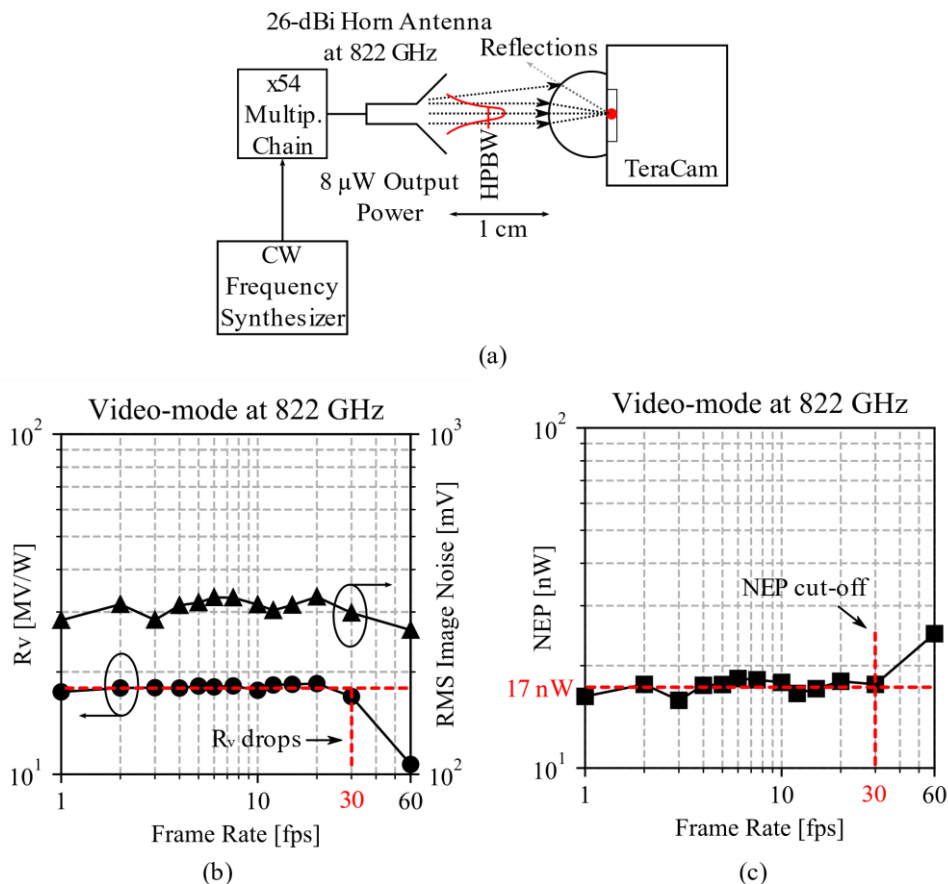


Fig. 8 (a) Measurement setup for determining the R_V through illuminating with a x54 multiplier chain coupled to a 26-dBi horn antenna with an output power of $8 \mu W$ in continuous wave mode (gain is not de-embedded from both noise and responsivity but later cancelled out by calculation of NEP), (b) RMS image noise and R_V and (c) averaged single pixel real-time NEP at 822 GHz for different frame rates with a typical value of $17 nW$.

The gain of the amplifiers on the camera PCB are not de-embedded from both R_V and noise but cancelled out for the NEP calculation. As the measurement results in Fig 6 (d) show, NEP trend is just varying slightly over an increased frame rate which can be explained by measurement inaccuracy. The minimum measured NEP is $15.81 nW$ for a frame rate of $10 fps$, the measured NEP at a frame rate of $30 fps$ is $17.61 nW$ and the typical averaged single pixel NEP for the chosen frame rates is $17 nW$. The slight variation can be explained by measurement inaccuracies. Due to the video bandwidth limitation of $150 kHz$ signal information gets (section 2.3) lost for $60 fps$ as visible in the dropping R_V value in Fig 6 (c) and thus, NEP also gets worse.

The finding of this measurement is that higher frame rates show a better NEP in the same integration time due to a relatively stable RMS image noise and R_V for different frame rates.

3.5 Integration mode and noise behavior

Typically, the accuracy and performance of thermal detectors can be improved by integrating over a long time period [15]. For the camera module this can be realized by frame averaging. In

the following this is examined for both operation modes, imaging and power metering, and it is explained in detail that this has to be considered in a different way with respect to the statistics. This section splits into sections where the noise behavior of both operation modes, power metering and imaging, are investigated separately.

3.5.1 Noise behavior in power meter mode

From previous investigations in section 3.1 we know that thermal noise is dominating in the camera module. Theoretically, the thermal noise can be reduced through averaging over a set of frames. This relation is verified in this section for operating the camera in the power meter mode where the typical video mode frame rate of 30 *fps* is chosen for measuring the RMS frame noise for different averages. In theory, an increased noise through selecting a larger number of pixels at the readout can be equalized by averaging over the same number of frames. This analysis gives us the optimum RMS frame noise of the camera module for both a single pixel and the whole 32 x 32-array.

To verify a decreased RMS frame noise for an increased average a measurement is performed where mean matrices with averages of $K = 2^m$, $m \in \{0,16\}$ are measured at a frame rate of 30 *fps* and finally saved into the measurement matrix A_{30fps} . Theoretically, the RMS frame noise should scale by the equation from [13]

$$\overline{\sigma_F} = \sqrt{\frac{1}{K} \sum_{k=1}^K \sigma^2_k} = \sqrt{\frac{1}{K} \sum_{i=1}^N \sum_{k=1}^K \sigma^2_{i,k}} = \sqrt{\frac{N}{K}} \cdot \sigma_k = \sqrt{\frac{\sigma_F^2}{K}}, \quad (8)$$

where K is the number of images for building the average and N is the number of the readout pixels. Thus, theoretically the NEP of the whole frame should come out to be the same as for a single pixel if we apply an average of $K = 1024$ to the frame. In many cases, the measurement time might not be too critical but signals might be extremely small. Hence, if there is an interest to detect these small signals the average can be increased. This analysis shows the NEP limitation of the camera module for selecting all of the 1024 pixels at the camera module and how this can be improved further. The RMS frame noise for increasing averaging factor is shown in a log-log plot in Fig 9 to investigate, if we can reach the same NEP for the whole array by averaging over 1024 frames.

Fig 9 (a) shows a visualization of the measurement routine and Fig 9 (b) the measurement results. The FPN cancellation is done once before measuring each 2D-matrix shown in Fig 9 (a) by measuring 1024 frames for the ‘Prev. Canc.’ (previous cancelled) results. For the ‘Periodic Canc’ results the FPN is cancelled out periodically during the measurement to avoid any kind of thermal drifts for large integration time measurements. Note that the measurement time for an average of

65k frames takes 33 minutes. Therefore, FPN- and measurement-matrices are measured iteratively for an average of 1024 frames. Then, FPN is cancelled out for each corresponding measurement matrix and the resulting matrices are reshape into a final matrix which contains 65k frames with periodically cancelled out FPN and finally, the average can be built in post-processing.

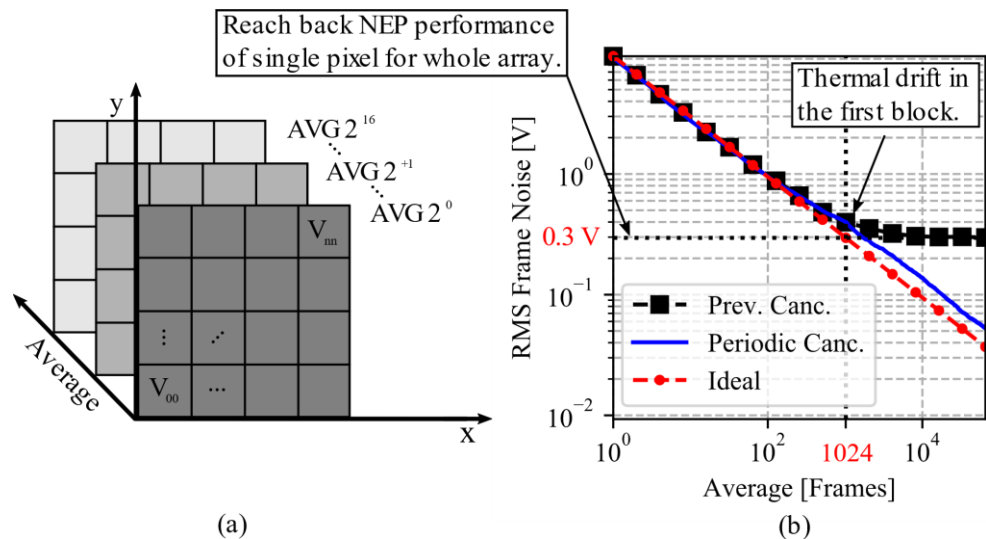


Fig. 9 (a) Measurement routine and (b) RMS image noise over average. For each measurement point a mean matrix is recorded. The noise trend versus average shows a linear behavior in the beginning and starts saturation then. The minimum reachable RMS image noise is around 9 mV for a single pixel and 288 mV for the whole array.

As shown in Fig 9 (b) the noise drops rapidly until an average factor of ≈ 100 and starts saturating then until it reaches a minimum RMS frame noise of around 300 mV for the whole 32×32 -pixel array and hence, the theory does not match to the measurement results completely if the FPN is cancelled out just once before the measurement. For $N = K$ the RMS frame noise should be similar to the performance of a single pixel but this is not the case in the measurements as we see a small gap for the RMS frame noise to the ideal trend line for an average of 1024 frames. Definitely, for larger frame average factors > 1024 this is not true. If the FPN is cancelled out periodically in the measurement this can be improved by avoiding any kind of thermal drifts and hence, the single pixel performance can be reached again. As a result of this investigation we conclude that that for larger integration periods the FPN should be cancelled out periodically, otherwise the noise saturates. With respect to this finding the thermal drift over time will be investigated in the last section.

The next section investigates the single pixel NEP improvement for long-term integration. This might give an indication if thermal drifts in long-period measurements are the reason for the saturation here.

3.5.2 Noise behavior in imaging mode

For using the imaging mode, each pixel is considered as a single sensing element and out of the pixel matrix an image is composed. We know from previous investigations in section 3.1.1, where we investigated the RMS pixel noise, that the pixel shows us a normally distributed behavior. From [15] we know that the sensitivity of thermal detectors can be improved through integrating over time.

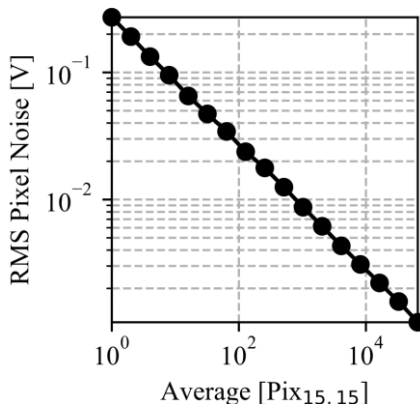


Fig. 10 RMS Pixel noise for integration mode in a log-log representation plot. The trend shows a linear behavior which results in a decreased NEP of $1/\sqrt{K}$ for averaging over K frames. This is only valid for using a single pixel and can be explained through noise reduction by adding gaussian sources.

To validate a non-limited noise reduction through averaging for a single pixel usable for imaging mode, a measurement is performed where just a single pixel is readout $2^{10} \cdot 2^{16}$ times. In post-processing, the same calculation is done as explained in previous section and the trend is shown in Fig 10. The trend shows a linear behavior which results in an improved NEP by $1/\sqrt{K}$ for averaging over K frames which means that the NEP can be improved a lot and this is very important for imaging, single pixel power metering and also for reference measurements by using the camera module as a multipixel power meter.

3.5 Mean offset and noise over time

The last important parameters for determining the optimum operation mode of the camera module are mean offset and noise trend over time. This is important because offsets are normally calculated once at the beginning of the measurement but this would not work for measurements with long integration periods because offsets would change over time due to thermal drifts. The trend over time is also an interesting parameter because device-heating can also have an influence on the noise performance of the on-chip detectors.

The time trend for the THz-Camera is characterized by a mean matrix, which is recorded

iteratively with an average of 4096 frames for a frame rate of 30 *fps*. The resulting matrix T_{30fps} , measured under a long integration period of five hours in a temperature-controlled environment, contains 135 matrices. The offset drift as well as the noise drift is extracted out of T_{30fps} for which the FPN is not cancelled out periodically to investigate the overall influence over the measurement time. Mean offset as well as mean RMS image noise is calculated for each of the 135 images, where mean offset is given by μ_k and RMS image noise by σ_k (see equation (4) and (5) in section 3.1.3). The measurement data is shown in the two-axis plot in Fig 11.

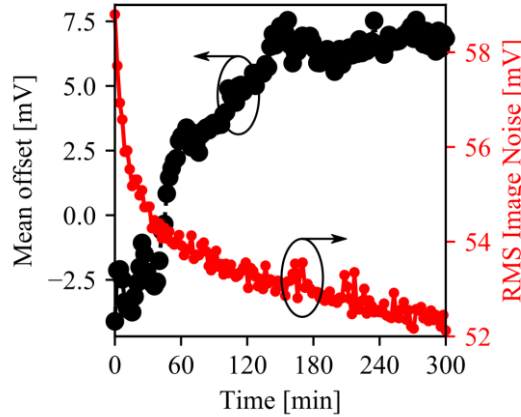


Fig. 11 Mean offset and noise trend over time for a long integration period of five hours. The offset varies just in a range of 400 percent and the RMS image noise decreases most in the first hour and hence, for very accurate measurements a warmup time of 60 *minutes* should be considered.

As a result of this investigation, we conclude that a warmup time of 60 *minutes* should be respected for the camera module in a temperature-controlled environment for optimum performance. The offset is drifting slightly over the whole measurement time and the total changes within five hours is 400 %, and the total noise change is ≈ 10 %. This investigation also explains why large integration times are broken up into smaller groups of 1024 frames (see section 3.5.1).

4. Conclusions

In this paper, the overall behavior of the image noise as generated in the 1k-pixel THz video camera has been experimentally investigated. In the context of such noise, the differences between two different operation modes of the camera, namely imaging mode and power-metering mode, have been quantitatively explained. The uncorrelated noise generated at the camera pixels show a Gaussian distribution and the sensitivity metric (i.e. NEP) of the camera is dependent on the RMS noise value. A typical minimum averaged single pixel real-time imaging NEP of $17 \text{ nW} \pm 10 \%$ is measured at 822 *GHz* for different frame rates. The averaged single pixel NEP for an integration time of one second for a frame rate of 30 *fps* is 3.1 *nW*. For further improvements to the camera

sensitivity, the following guidelines are suggested for the camera operation. When operating the camera in imaging mode, noise for each pixel should be individually minimized by pixel level offset calibration and pixel-level integration of image frames in time. For power-metering mode, where a higher sensitivity is targeted with a long integration time, offset cancellation must be done periodically to cancel the low-frequency noise components related to thermal drifts inside the camera circuitry. Also, a faster integration towards high sensitivity can be achieved by a selective acquisition of desired pixels from the camera frame (i.e. clipping window). In this paper, we have experimentally demonstrated that the NEP improvements with frame integration and clipping window follow the standard statistical treatment of independent random variables, i.e. single pixel NEP is typically scaled by $\sqrt{K/N}$ where K is the number of pixels in the clipping window and N is the number of frames that are integrated over time. Therefore, a single pixel NEP of 100 pW can be achieved by averaging noise samples over 31 seconds integration period at 30 fps which corresponds to a 930 frames integration measurement.

The directivity distribution of camera pixels is also experimentally characterized. Experimental results show that directivity quickly rolls-off for pixels away from the FPA center due to the off-axis aberrations induced by the hyper-hemispherical silicon lens. Due to a circular lens aperture, the directivity roll-off is most pronounced at the corner pixels of the FPA, which show a reduced directivity by around 10 dBi as compared to the center camera pixels. This effect should be calibrated during power or image measurements with the camera for a higher accuracy.

The noise behavior associated with camera start-up is also reported. It is observed that about 10% larger noise is generated during the camera start-up, and this noise subsides over time. This can be attributed to the heat diffusion inside the camera chip. Therefore, a camera warm-up period lasting around an hour should be respected for high sensitivity measurements. Our results also suggest that measurements inside a temperature-controlled environment can further help in extracting a better sensitivity out of the THz camera.

Acknowledgement

The authors would like to thank TicWave GmbH, Germany, for support and for providing the camera module for the performance characterization in this paper.

References

- [1] P. H. Siegel. "Terahertz technology". *IEEE Transactions on microwave theory and techniques*, 50, 3, 910-928 (2002).

- [2] R. Al Hadi, H. Sherry, J. Grzyb, et al. "A 1 k-pixel video camera for 0.7–1.1 terahertz imaging applications in 65-nm CMOS". *IEEE Journal of Solid-State Circuits*, 47, 12, 2999-3012 (2012).
- [3] C. am Weg, W. von Spiegel, B. Hils, et al. "Fast active THz camera with range detection by frequency modulation". in *Infrared, Millimeter and Terahertz Waves (2008). IRMMW-THz (2008). 33rd International Conference on (2008)*.
- [4] A. Lisauskas, W. Von Spiegel, S. Boubanga-Tombet, et al. "Terahertz imaging with GaAs field-effect transistors". *Electronics Letters*, 44, 6, 408-409 (2008).
- [5] U. R. Pfeiffer, Y. Zhao, J. Grzyb, et al. "A 0.53 THz reconfigurable source module with up to 1 mW radiated power for diffuse illumination in terahertz imaging applications". *IEEE Journal of Solid-State Circuits*, 49, 12, 2938-2950 (2014).
- [6] R. Jain, J. Grzyb and U. R. Pfeiffer. "Terahertz light-field imaging". *IEEE Transactions on Terahertz Science and Technology*, 6, 5, 649-657 (2016).
- [7] S. Malz, R. Jain and U. R. Pfeiffer. "Towards passive imaging with CMOS THz cameras". in *Infrared, Millimeter, and Terahertz waves (IRMMW-THz), 2016 41st International Conference on (2016)*.
- [8] D. Headland, P. Hillger, R. Zatta and U. Pfeiffer. "Incoherent, spatially-mapped THz spectral analysis". *IRMMW-THz (2018)*.
- [9] TicWave, *Product portfolio (2018)*.
- [10] J. R. Barry, E. A. Lee and D. G. Messerschmitt. Digital communication. Springer Science & Business Media (2012).
- [11] D. F. Filipovic, S. S. Gearhart and G. M. Rebeiz. "Double-slot antennas on extended hemispherical and elliptical silicon dielectric lenses". *IEEE Transactions on microwave theory and techniques*, 41, 10, 1738-1749 (1993).
- [12] D. F. Filipovic, G. P. Gauthier, S. Raman and G. M. Rebeiz. "Off-axis properties of silicon and quartz dielectric lens antennas". *IEEE Transactions on Antennas and Propagation*, 45, 5, 760-766 (1997).
- [13] H. Kuchling. Taschenbuch der physik. Deutsch, 574-575 (1988).
- [14] J. Mazzetta, D. Caudle and B. Wageneck. "Digital camera imaging evaluation". *Electro Optical Industries*, 8 (2005).
- [15] V. Radeka. "Low-noise techniques in detectors". *Annual Review of Nuclear and Particle Science*, 38, 1, 217-277 (1988).
- [16] M. C. Kemp. "Explosives detection by terahertz spectroscopy—a bridge too far?". *IEEE Transactions on Terahertz Science and Technology*, 1, 1, 282-292 (2011).
- [17] F. Friederich, W. Von Spiegel, M. Bauer, et al. "THz active imaging systems with real-time capabilities". *IEEE Transactions on Terahertz Science and Technology*, 1, 1, 183-200 (2011).
- [18] K. B. Cooper, R. J. Dengler, N. Llombart, et al. "THz imaging radar for standoff personnel screening". *IEEE Transactions on Terahertz Science and Technology*, 1, 1, 169-182 (2011).
- [19] W. L. Chan, K. Charan, D. Takhar, et al. "A single-pixel terahertz imaging system based on compressed sensing". *Applied Physics Letters*, 93, 12, 121105 (2008).
- [20] Y. Yang, M. Mandehgar and D. R. Grischkowsky. "Broadband THz pulse transmission through the atmosphere". *IEEE transactions on terahertz science and technology*, 1, 1, 264-273 (2011).
- [21] Z. D. Taylor, R. S. Singh, D. B. Bennett, et al. "THz medical imaging: in vivo hydration sensing". *IEEE transactions on terahertz science and technology*, 1, 1, 201-219 (2011).
- [22] K. Tanaka, H. Hirori and M. Nagai. "THz nonlinear spectroscopy of solids". *IEEE Transactions on Terahertz Science and Technology*, 1, 1, 301-312 (2011).
- [23] C. Kulesa. "Terahertz spectroscopy for astronomy: From comets to cosmology". *IEEE Transactions on*

- Terahertz Science and Technology*, 1, 1, 232-240 (2011).
- [24] K. Ajito and Y. Ueno. "THz chemical imaging for biological applications". *IEEE Transactions on Terahertz Science and Technology*, 1, 1, 293-300 (2011).
- [25] K. Ajito, H.-J. Song, A. Hirata, et al. "Continuous-wave terahertz spectroscopic imaging at over 1 THz for pharmaceutical applications". in *Infrared Millimeter and Terahertz Waves (IRMMW-THz), 2010 35th International Conference on* (2010).
- [26] N. Shimizu, T. Ikari, K. Kikuchi, et al. "Remote gas sensing in full-scale fire with sub-terahertz waves". in *Microwave Symposium Digest (MTT), 2011 IEEE MTT-S International* (2011).
- [27] N. Sarmah, J. Grzyb, K. Statnikov, et al. "A fully integrated 240-GHz direct-conversion quadrature transmitter and receiver chipset in SiGe technology". *IEEE Transactions on Microwave Theory and Techniques*, 64, 2, 562-574 (2016).